Volume 11
Number 1
1 January 2026
Pages 1–140

# MSDE

Molecular Systems Design & Engineering

rsc.li/molecular-engineering

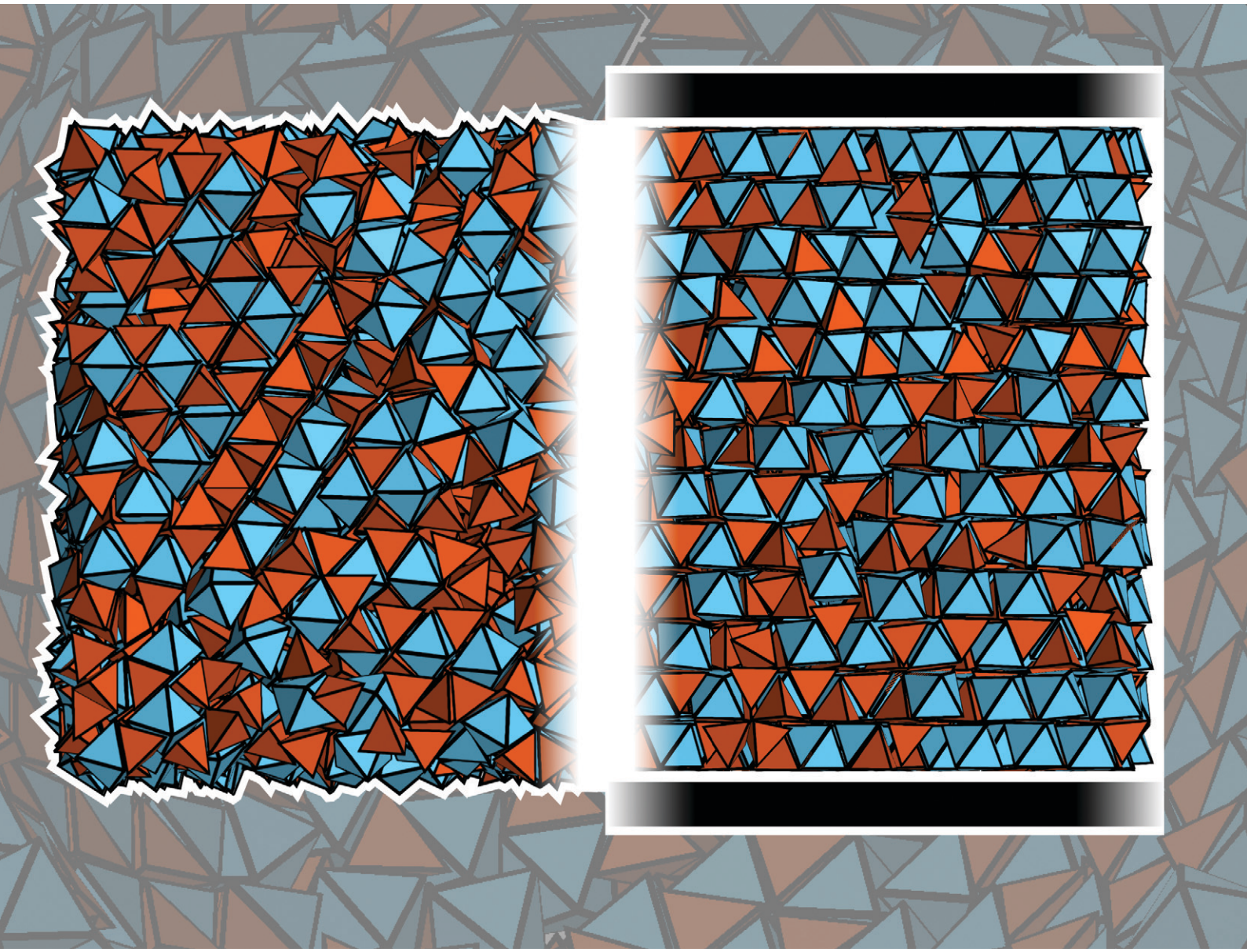

ISSN 2058-9689

ROYAL SOCIETY OF CHEMISTRY

**PAPER**

Julia Dshemuchadse *et al.*

Advancing the self-assembly of binary colloidal crystals of tetrahedra and octahedra with confinement

10 YEARS ANNIVERSARY IChemE

MSDE

PAPER

View Article Online
View Journal | View Issue



Cite this: *Mol. Syst. Des. Eng.*, 2026, 11, 62

# Advancing the self-assembly of binary colloidal crystals of tetrahedra and octahedra with confinement

Nathan C. Huang, Rachael S. Skye and Julia Dshemuchadse *

Received 4th June 2025,
Accepted 27th October 2025

DOI: 10.1039/d5me00092k

rsc.li/molecular-engineering

Photonic crystals can be self-assembled from binary colloidal dispersions, but the robust assembly of high-quality crystals in quantities sufficient for large-scale applications remains challenging. Here, we study the assembly of polyhedral colloidal nanoparticles at surfaces with spherical and flat-wall geometries to examine the influence of confinement on the process and products of crystallization compared to the bulk. We find that confinement improves crystallization at non-ideal stoichiometries but does not lower the minimal packing fraction at which crystallization occurs. Crystals formed in confinement exhibit higher degrees of crystallinity and lower quantities of secondary-phase defects: the formation of well-ordered layers and shells appears to be promoted by flat walls and spherical container interfaces. These findings demonstrate the potential for enhanced control over the synthesis of novel materials with tailored structures and properties for photonic applications.

**Design, System, Application**

Colloidal particles have been fabricated from a wide range of materials and can be self-assembled into a myriad of structures. Colloidal crystals allow access to materials design at a length scale that is difficult and costly to tackle with conventional manufacturing techniques, and because the size of colloids is on the order of magnitude of the wavelength of visible light, colloidal crystals have proven useful in photonic applications. However, it remains challenging to produce the large, low-defect crystals that are necessary for high-quality photonic devices, and the kinetic difficulties are even more pronounced in complex systems, for example consisting of multiple particle components. In this work, we investigate the targeted synthesis of binary colloidal crystals *via* confinement. Through the introduction of flat and curved surfaces, heterogeneous nucleation of the crystal is encouraged. The match between the surface geometry and the structure of the colloidal crystal allows us to minimize defects in the binary assembly and to stabilize its crystallization across densities and stoichiometries. This approach will allow for an improved synthesis route for colloidal crystals, enabling their translation to commercial application.

## 1 Introduction

Colloidal crystals emerge on the nanometer length scale through spontaneous self-assembly of nanoparticles into well-defined structures. Such ordered metamaterials have unique applications arising from the length scale that they inhabit, ranging from dozens to hundreds of nanometers, especially in optical devices such as photonic crystals. Materials design on the colloidal length scale allows for the creation of tunable photonic crystals, but in turn it requires that a diverse range of structures from materials with contrasting refractive indices be assembled successfully.

Photonic crystals can be created through the contrast between a material and air—both in the form of direct photonic crystals, in which particles form the crystal, as well as inverse crystals, in which air pockets form the crystal within a matrix of material—or they can be made from a space-tessellating mixture of multiple types of particles.[1] However, while self-assembly has garnered interest as a promising low-cost and low-energy method for fabricating photonic crystals, a scalable implementation of this technique has not yet been achieved due to the difficulty of synthesizing sufficiently large crystals at low defect densities.[2]

Prior work has primarily focused on one-component colloidal crystals. There are generally two methods for designing building blocks for crystal structures on the colloidal length scale: enthalpy-stabilized crystals assembled through attractive forces such as DNA linkers or dipole interactions[3–5] and entropy-stabilized crystals formed from packing building blocks, with structure primarily controlled by the particle shape.[6–10] Colloids with weak, short-range interactions are often treated as effectively "hard" particles.

In order to further modify the crystal assembly, confinement can be introduced experimentally through different synthesis

*Department of Materials Science and Engineering, Cornell University, Ithaca, NY 14853, USA. E-mail: jd732@cornell.edu*

methods, such as deposition on a substrate[11,12] or assembly within emulsion droplets.[13,14] Previous work has shown that confinement can have a large impact on the structures that self-assemble in one-component systems, including changing the phase behavior and crystallization kinetics[14–16] and affecting the orientation of anisotropic particles.[17–20]

Binary crystals—assembled from two distinct types of particles—allow for a wider range of properties based on the interaction of two distinct materials, including crystals formed *via* random substitution,[21] enthalpy-stabilized systems,[22] size-disperse colloid packings,[23] and systems composed of two different anisotropic particles.[23–28] Binary colloidal crystals have been theorized to have useful photonic properties, including a wide bandgap in the wavelength range of visible light.[23,29] Furthermore, if binary crystals can be assembled robustly, they offer the opportunity to selectively dissolve one type of building block, leaving behind a new crystal structure formed by the remaining components.[30,31] However, understanding the wide design space offered by binary crystals is a challenge. The self-assembly of hard polyhedral particles has been computationally investigated extensively in the bulk,[32–34] yet there are—to the best of our knowledge—no previous studies of how binary systems behave in confinement.

To begin to use confinement as a tool to control binary crystal assembly, we analyze a simple binary crystal of polyhedra that forms from a 2 : 1 mixture of regular tetrahedra and octahedra with identical edge lengths and crystallizes into a space-tessellating structure.[28] Unlike other space-tessellating honeycombs,[27] the tetrahedra–octahedra honeycomb has been observed to spontaneously self-assemble,[28] rendering it an ideal target for initial studies of binary systems. In addition, both of the component shapes can be synthesized experimentally, for example as nanoscopic octahedra made up of silver or gold,[11,35,36] copper,[37] or oxide materials such as $CeO_2$,[38] and as tetrahedra made up of gold,[39] polystyrene,[40] and semiconductors such as cadmium sulfide.[41] Here, we use simulations to investigate how confinement changes the self-assembly behavior of two-component systems of tetrahedra and octahedra. Through this work, we will build an understanding of how to direct the structure of colloidal crystals and use the assembly conditions to optimize for the self-assembly of high-quality photonic crystals.

## 2 Methods

We investigate binary colloidal systems of tetrahedra and octahedra *via* hard-particle Monte Carlo (HPMC) simulations implemented using the HOOMD-blue package.[42–45] In the hard-particle model, no explicit forces act between particles, and self-assembly is entirely driven by volume exclusion and the emergence of directional entropic forces.[46–48] Such hard particles can model colloids at nanometer to micrometer length scales with weak, short-range interparticle interactions.[49] Simulation data was managed with signac,[50–52] and assembled structures were analyzed using freud.[53,54] Visualizations were created using OVITO[55,56] and plato.[57]

Tetrahedral and octahedral particles are defined as polyhedral shapes with equal edge lengths. Systems contain $N = 4096$ particles, with a near-ideal stoichiometry of 65% tetrahedra and 35% octahedra. The HPMC simulations follow a procedure that was previously established for one-component systems.[18] The system is compressed in an NPT ensemble by increasing the pressure exponentially from $\beta P = 1$ to $\beta P = 400$ over $2 \times 10^6$ Monte Carlo steps, where $\beta = 1/k_B T$. Once a targeted packing fraction $\phi$ is reached, compression stops and the system is allowed to equilibrate for $10^5$ Monte Carlo steps. The structure of the system at the end of the equilibration stage is then analyzed. Throughout the compression phase, the acceptance ratio of Monte Carlo moves is maintained at 20% by adjusting the step sizes of compression, particle moves, and particle rotations.[58]

Self-assembled systems are investigated at varying packing fractions, stoichiometries (*i.e.*, tetrahedra-to-octahedra ratios), and confinement geometries. Packing fractions are sampled between $\phi = 0.5$ and 0.8 (in increments of $\Delta\phi = 0.05$). System stoichiometries with 50% to 80% tetrahedra are simulated (in increments of $\Delta = 5\%$). Two confinement geometries are investigated, implemented *via* the addition of spherical and flat hard walls into the HPMC simulation (see Fig. 1). For spherical confinement, a single wall encompasses all particles in the simulations from the start and is subsequently shrunken to pressurize the system. For flat-wall confinement, two walls are placed with a slight offset from the simulation box boundaries on one pair of opposing faces of the simulation box, and they

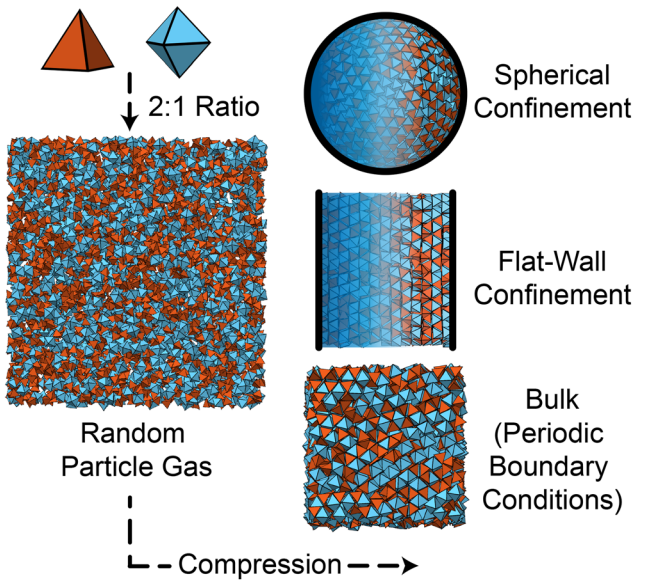


**Fig. 1** Systems of 2/3 tetrahedra and 1/3 octahedra, initialized as a random gas of hard particles, are compressed in three different geometries: spherical confinement (a spherical wall encapsulating all particles), a flat-wall confinement (a flat wall in one spatial dimension and periodic boundaries in the two remaining dimensions), or a bulk system with periodic boundary conditions in all three dimensions.

are moved closer together to simulate pressurization (the remaining faces of the simulation box maintain periodic boundary conditions). In bulk systems and systems with flat-wall confinement, a "floppy-box" mechanism is activated when a packing fraction of $\phi = 0.3$ is reached, allowing the system box to shear and adjust its aspect ratio. This mitigates the impact of constraints imposed by the periodic boundary conditions on self-assembly structures, which penalizes structures that are incommensurate with the original simulation box.[59] The "floppy box" mechanism is deactivated during the equilibration stage of the simulation.

For bulk simulations, preliminary studies found that an additional hold at $\beta P = 36$ for $3 \times 10^6$ steps was necessary to provide sufficient time for crystals to nucleate. The average time for homogeneous nucleation is higher than for heterogeneous nucleation at walls; in order to form structures of comparable quality, a much longer time was needed in the bulk.[60] Gas and crystalline references are simulated using modified compression processes: the gas reference is simulated by ending the compression at a low packing fraction ($\phi = 0.1$); the crystal reference is simulated by compressing to a packing fraction of $\phi = 0.75$ and doubling the number of equilibration steps at each point along the pressure ramp.

# 3 Results and discussion

## 3.1 Interparticle distances

Three phases were observed in the system after compression. The single-component octahedra phase self-assembles into a distorted body-centered cubic structure,[28,35] the single-component tetrahedra phase self-assembles with quasicrystal-like motifs,[61] and the binary crystal of tetrahedra and octahedra self-assembles into the space-tessellating honeycomb—the face-centered cubic fluorite structure type.[28] For each of these phases, we identify the characteristic interparticle distances, and by comparing the frequency of these structure-specific pairwise distances, we identify which phases are present and estimate their relative occurrence—the phase fractions. In single-component phases, tetrahedron–tetrahedron pairs exhibit interparticle distances between $r = 0.5$ and 0.75 and octahedron–octahedron pairs have interparticle distances between $r = 1.515$ and 1.5. Tetrahedron–octahedron pairs in the binary crystal exhibit characteristic interparticle distances between $r = 0.75$ and 1.0.

Radial distribution functions (RDFs)—quantifying the average density of particles as a function of interparticle distance—are shown in Fig. 2 for simulations of both the bulk and confined geometries. At a packing fraction of $\phi = 0.5$, the particles fail to crystallize in the bulk: the RDF shows a broad distribution of interparticle distances without a distinct peak, indicating the presence of a fluid phase. When in spherical or flat-wall confinement, similarly broad RDFs are observed; while a peak emerges around $r = 0.9$—indicative of the expected tetrahedron–octahedron motif in the binary crystal—the relatively low peak intensity signifies

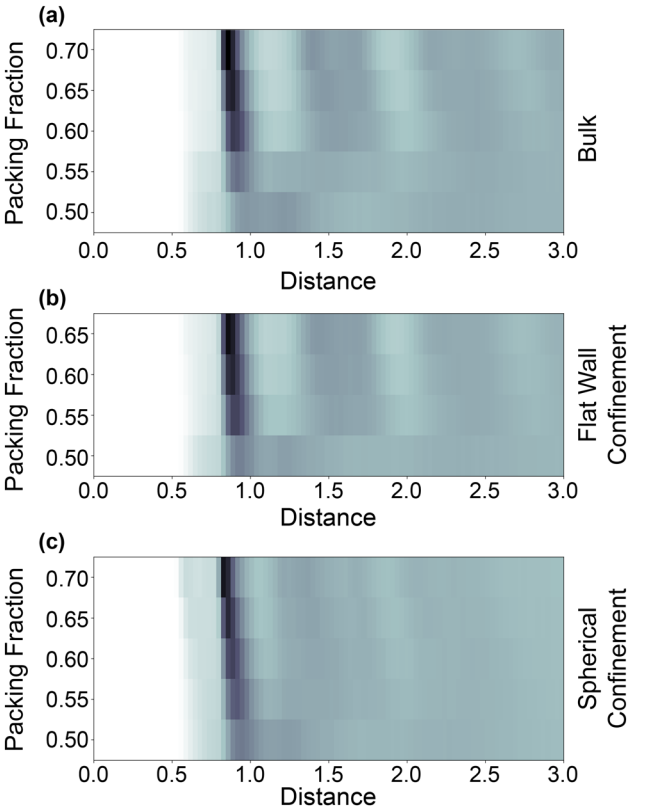


Fig. 2 Radial distribution functions of systems of hard tetrahedra and octahedra self-assembled in (a) bulk, (b) flat-wall confinement, and (c) spherical confinement geometries. The plotted intensities correspond to the relative density of particles on a linear scale normalized to the highest density within each type of system.

that this is not yet a dominant phase in the system (see Fig. S1 in the SI for RDFs separated by particle type).

At packing fractions of $\phi = 0.55$ and higher, the particles crystallize into the binary crystal. As the packing fraction is increased, the peaks associated with the binary crystal become narrower and move to lower interparticle distances, approaching $r = 0.75$—the optimal interparticle distance in a densely-packed, perfect crystal. We also observe additional RDF peaks corresponding to the second- and third-nearest-neighbor environments in the binary crystal structure at $r \approx 1.5$ and 2.25, indicating long-range order.

Fig. 3 quantifies the amount of particle pairs corresponding to the binary crystal for the bulk, flat-wall confined, and spherically confined systems across varying packing fractions and varying stoichiometries. The crystallinity of systems in flat-wall confinement reaches the same values at high packing fractions ($\phi = 0.65$–0.70), but the flat-wall confined systems are measurably more crystalline at low packing fractions ($\phi = 0.55$–0.60) (see Fig. 3a). While the spherically confined systems exhibit a higher frequency of binary crystal motifs at low packing fractions ($\phi = 0.50$–0.55), these values fall below the bulk systems at larger packing fractions, which indicates that the confining wall serves as a template for the formation of these motifs at low densities, but that its curvature prevents the

 

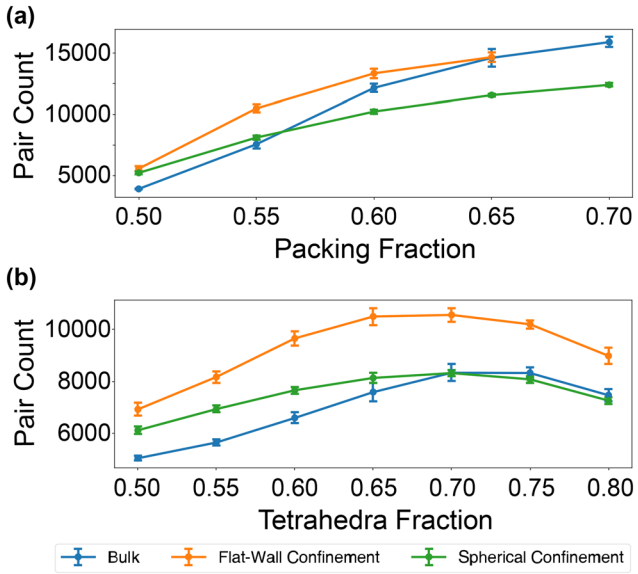


Fig. 3 Number of tetrahedron–octahedron neighbor pairs at distances indicating the formation of the binary crystal—a proxy for crystallinity—(a) varying with packing fraction at the ideal stoichiometry and (b) varying with stoichiometry at $\phi$ = 0.65 packing fraction.

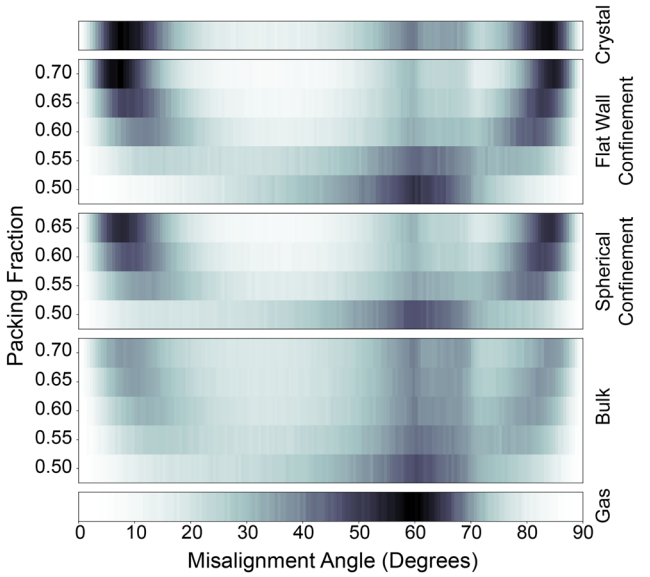


Fig. 4 Misalignment angles of tetrahedra in (top to bottom): a crystalline-phase reference, flat-wall confinement, spherical confinement, bulk, and a gas-phase reference (corresponding to the random "shark-fin" distribution). Peaks at 0° and 90° correspond to the ideal binary crystal; peaks at 70.5° correspond to tetrahedra-rich defects and stacking faults. The feature at 60° is caused by the underlying "shark-fin" distribution (compare to gas-phase distribution) (possible misalignment angles for tetrahedra range from 0° to 90°, due to the particle's point group symmetry $\bar{4}3m$).

crystallization of a larger proportion of the system at high densities. With the introduction of flat-wall confinement, larger binary crystals with higher crystallinity form, exhibiting fewer defects corresponding to the competing single-component phases (see also Fig. S2 for data on all motif types).

Flat-wall confinement leads to the highest proportion of correct tetrahedra–octahedra motifs around the ideal tetrahedra fraction of 67% (see Fig. 3b). In both confined geometries, the proportion of correct tetrahedra–octahedra motifs peaks around the ideal value—between 65–70%—whereas bulk simulations seem to exhibit a maximum proportion of correct motifs at tetrahedra fractions between 70–75%, indicating that an over-stoichiometry of tetrahedra is required in the bulk—a similar effect had previously been reported in systems of binary systems of repulsive spherical particles.[62]

### 3.2 Angular particle (mis)alignments

A second measure of crystallinity is based on the misalignment angle between neighboring particles, *i.e.*, the smallest rotation around an arbitrary axis to change the orientation of one particle to match that of the other. In the gas phase, particles are randomly oriented, and the misalignment angle distribution follows a random "shark-fin" distribution, which arises due to the particle symmetry[63] (due to the different polyhedral symmetries of tetrahedra and octahedra—$\bar{4}3m$ and $m\bar{3}m$, respectively—only pairs of polyhedra with the same shape are analyzed with respect to their misalignment). The binary tetrahedra–octahedra crystal exhibits three characteristic misalignment angles: octahedra pairs have a misalignment of 0°, while tetrahedra pairs have misalignments of 90° and 0°—for edge- and vertex-sharing neighbors, respectively. Face-sharing tetrahedra have a characteristic misalignment of ~70.5°, and they occur in two types of defects: the one-component phase composed of only tetrahedra, and stacking faults in the binary crystal. The misalignment angle distributions for tetrahedra and octahedra are shown in Fig. 4 and 5, respectively.

At the lowest simulated packing fraction ($\phi$ = 0.5), the misalignment angle distributions in bulk and in confinement closely resemble the distribution of the gas reference. In the bulk simulations, the misalignment angle distributions approach the distribution of the crystal reference, but they remain very broad even at higher packing fractions, which signals poor crystallinity of the resulting structure.

When in spherical confinement, the misalignment angle distributions narrow, especially at higher packing fractions, indicating a higher prevalence of crystalline motifs compared to the bulk. In contrast with the trend in relative distances (Fig. 3), by this measure spherical confinement dramatically increases the quality of the crystal. We propose that this effect is due to the curvature of the sphere: the relative distances in interparticle motifs distort to accommodate the curved surface, while retaining the same misorientation. Additionally, the single-component octahedral defect has the same signature misorientation angle as the binary crystal, and thus this defect is not reflected in analysis of the misalignment.

In flat-wall confinement, the misalignment angle distribution narrows further compared to the bulk and

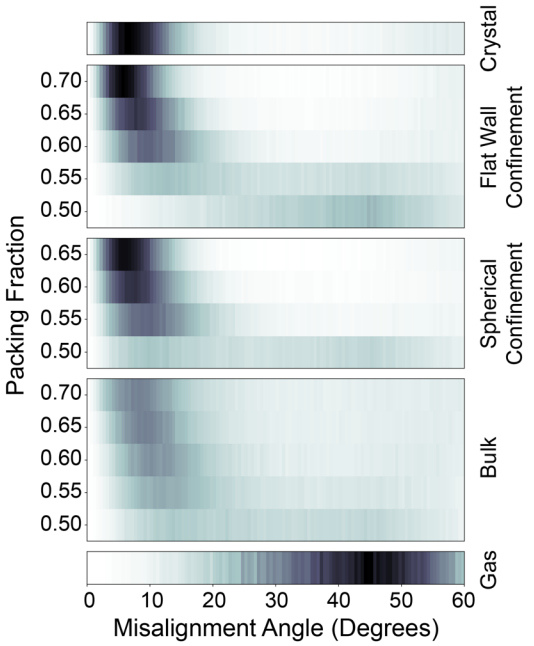


Fig. 5 Misalignment angles of octahedra in (top to bottom): a crystalline-phase reference, flat-wall confinement, spherical confinement, bulk, and a gas-phase reference. The ideal crystal exhibits particle misalignments of 0° (possible misalignment angles for octahedra range from 0° to 60°, due to the particle's point group symmetry $m\bar{3}m$).

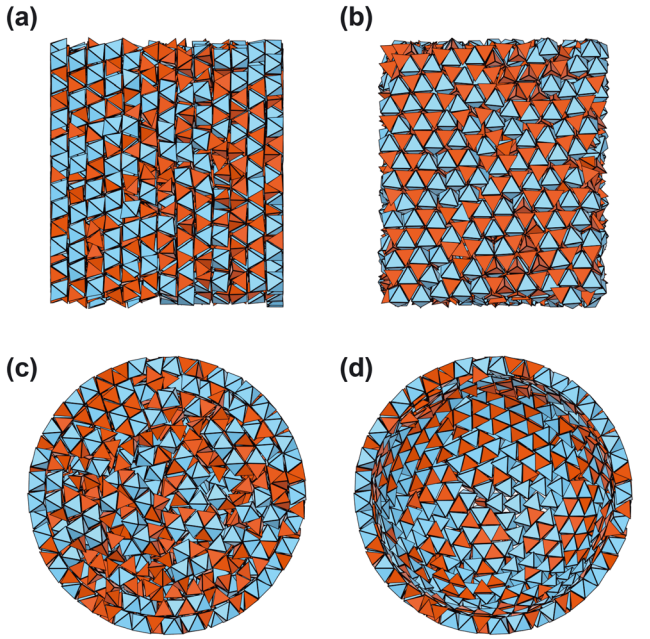


Fig. 6 Cross-sections of self-assembled systems: in flat-wall confinement (a) orthogonal to the walls and (b) parallel to walls, and in spherical confinement showing (c) the full system and (d) the outermost shell isolated.

spherical confinement geometries, indicating a well-formed crystal. As there is no curvature enforced by the wall, the misalignment shows strong, narrow peaks that match the ideal binary assembly.

### 3.3 Self-assemblies in relation to confinement geometries

Visualization of the assemblies shows that distinct, flat layers form in flat-wall confinement, and concentric shells—*i.e.*, curved layers—form in spherical confinement. These layers contain one shear plane of the crystal structure. In Fig. 6, cross-section views of structures obtained in flat-wall and spherical confinements are shown. When confined by flat walls, particles form layers parallel to the container walls, extending across the entire system. When in spherical confinement, particles form up to three distinct concentric shells near the interface with the container, and a more disordered region forms at the core. Shells closer to the center of the container have higher curvature, so it is likely that, for a system of $N = 4096$ particles, only three shells can be formed before the increasing curvature prevents the formation of additional shells, suggesting that higher numbers of shells could be formed in larger systems.

The development of layers and shells in confinement can be studied in more detail using modified RDFs, in which we quantify the distribution of interparticle distances relative to fixed, geometry-specific reference points in the system. The modified distribution for flat-wall confinement defines the central plane of the container—parallel to the walls—as $r = 0$, and interparticle distances are projected on the axis that is oriented perpendicularly to the wall. This generates a density plot of particle positions perpendicular to the confining walls. In systems in spherical confinement, the RDF is modified such that the center of the spherical container is defined as $r = 0$ and the distribution of particles is measured radially from the center. These container-centered distribution functions are shown in Fig. 7. For systems in spherical confinement, curvature increases and surface area decreases as shells form closer to the center of the system. As a result, the number of particles per shell decreases moving inwards from the container interface. Closer to the center of the spherical container, the system exhibits less distinct bands.

Bands consist of three peaks, highlighting the formation of individual layers of the binary crystal: the peaks correspond to the three particle positions that make up the unit cell, showing a sequence of tetrahedra–octahedra–tetrahedra, according to their centers of mass. In each system, the outermost bands exhibit sharper peaks, indicating a higher degree of crystallinity near the container interface. Notably, at the lowest packing fraction of $\phi = 0.5$, these bands still form near the interface with the container despite a low degree of crystallinity at the center of the container. This highlights the impact of the container walls on the self-assembly behavior of the tetrahedra and octahedra: crystals appear to nucleate at the interface with the container, which results in the formation of a layered structure that conforms to the orientation of the walls. This observation is confirmed by examining the evolution of the particle distribution over time, which shows that distinct layers form sequentially starting at the walls and moving inwards (see Fig. S5 and S6 in the SI).

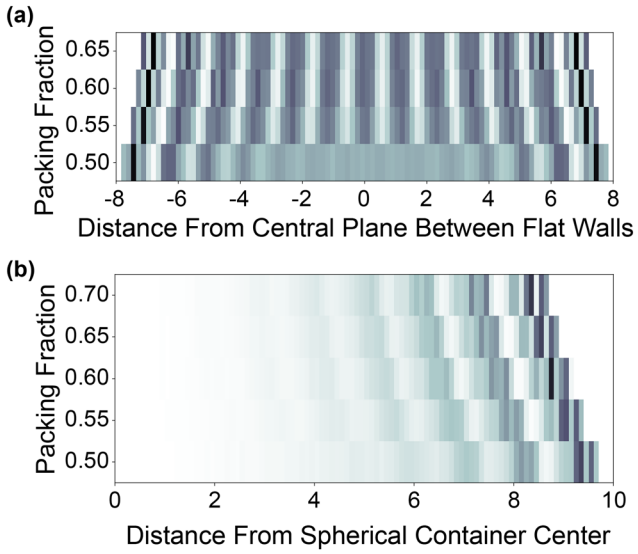


**Fig. 7** Distribution of particles (a) in flat-wall confinement, perpendicular to the walls, and (b) in spherical confinement, as a function of the distance from the container center. The relative density of particles is plotted on a linear scale.

Heterogeneous nucleation at confining walls is consistent with observations made in systems of hard spheres,[64] whose crystalline phases also exhibit dense layers of particles that conform with flat interfaces. The opposite effect was observed in binary systems of spheres,[16] which form Frank–Kasper phases that do not exhibit densely packed, flat layers in their crystal structure that could form at an interface. These different cases suggest that heterogeneous nucleation occurs when the self-assembled structure at the interface matches that of the nucleating structure (*e.g.*, in this study and in dense sphere packings[64]) and that it does not occur when no such match exists (*e.g.*, in binary sphere packings[16]). This non-trivial relationship between the crystallization mechanism, the crystallizing structure, and the geometry of the confining interfaces should be subject to future studies.

Finally, examining the layered structures shows that it is not possible for spherical shells to crystallize the tetrahedra–octahedra honeycomb without defects. In all spherical systems, "scarring" caused by the curvature is observed.[65,66] In this case, scarring appears to be dominated by octahedra, which matches the increased occurrence of the characteristic octahedron–octahedron interparticle distances ($r$ = 1.15–1.5) in RDFs of systems in spherical confinement in Fig. 2 (this is corroborated by the increased presence of octahedron–octahedron defects at the surface, quantified in Fig. S7 and visualized in Fig. S8 in the SI).

In addition, while the individual layers are well-crystallized, these concentric shells are not commensurate, *i.e.*, the translational symmetry of the tetrahedra–octahedra honeycomb is not strong in the radial direction. Each layer contains one complete shear plane of the crystal, and particle volumes are fully contained within one plane, rendering the inter-layer interactions weak. Similar effects are seen in other systems of confined polyhedra[18,67] and in liquid crystals formed from faceted polyhedra, with particles demonstrating strong orientational order in layers but no overall translational order.[6,68] Here, this suggests that each formed layer acts as a new interface that allows for the following layer to form, meaning that they essentially represent independent and consecutive nucleation events. In spherical confinement, this behavior is in contrast to systems of hard spheres, whose layers interpenetrate slightly and are often observed to form grains in a symmetric icosahedral arrangement.[64,69]

# 4 Conclusions

In this study, the self-assembly behavior of tetrahedra and octahedra in confinement was investigated *via* hard-particle Monte Carlo simulations. The effect of flat-wall and spherical confinement on the self-assembled structures of systems of polyhedra provides an opportunity to propose synthesis conditions that can render higher-quality binary colloidal crystals compared to bulk systems. Confinement in either geometry catalyzes the formation of crystals at lower packing fractions, resulting in higher crystallinity at intermediate packing fractions compared with the bulk. Additionally, crystallization in the confined system proceeds more quickly, with the bulk crystals requiring a simulation 150% longer than confined crystals to form structures with a comparable —and sometimes still lesser—degree of order.

Container interfaces provide sites to nucleate crystals, resulting in well-formed layers or shells conforming to the geometry of the container. This effect is commonly observed in repulsive or hard-particle systems,[11,12,15,67,70] and nucleation at interfaces is also commonly observed among systems with a wide range of interparticle interactions.[4] We find that spherical confinement introduces additional topological defects due to the curvature introduced into the nucleated layers, which are flat in the formed bulk structure. By matching their geometry, the binary crystals assembled in flat-wall confinement exhibited lower defect concentrations compared with the bulk. Confinement also induced crystallization at less-ideal stoichiometries compared to the bulk and suppressed the formation of single-component defect phases—effectively stabilizing the binary compound phase with respect to variations in stoichiometry.

This work will guide future research into colloidal crystallization, demonstrating how binary systems can be tuned *via* confinement geometry. In particular, while the tetrahedra–octahedra binary system has been observed to self-assemble without confinement, other space-filling binary structures have not.[27] We propose that it may be possible to induce crystallization of additional honeycombs *via* confinement and interfaces, expanding the range of structures available for building functional devices.

The here-studied system allows for multiple routes to produce interesting photonic crystals. Firstly, the tetrahedra–octahedra honeycomb assembles the fluorite structure type, which is composed of two sublattices that could be isolated

by dissolving one of the two components, which would in turn allow access to particularly low-density structures.[30] The octahedra form a face-centered cubic sublattice, which could be backfilled to form inverse opal. The tetrahedra form a particularly low-density simple cubic structure, which can similarly be used to template the inverse simple cubic structure. Both inverse structures, as well as the parent fluorite, can exhibit a wide photonic band gap as a function of the difference in refractive index between the constituent materials.[1] Alternatively, if sufficiently high-contrast particles can be synthesized, no dissolution step may even be necessary.

Additionally, the observation of topological scar defects being dominated by one component is a distinct defect type that is specific to multi-component assembly and different from previously studied one-component systems, such as hard spheres[69] or tetrahedra.[18]

Future studies should investigate how other structures form in the presence of interfaces, in particular if their self-assembled structures contain densely-packed motifs that are congruent with the interfacial geometry, as is the case for flat walls and the densely packed flat layers of the tetrahedra–octahedra honeycomb. The intersection between system stoichiometry and topology appears to be particularly interesting: are different species better suited to accommodating curvature and how are crystallinity, stoichiometry, and structure affected as a result? The resulting insights will inform future work in fabricating low-defect colloidal crystals for proposed applications in photonic devices, in particular in multi-component systems in which a high degree of crystallinity is difficult to achieve, and the strategic employment of surface-mediated nucleation can serve as a powerful synthetic tool.

## Author contributions

N. C. H., R. S. S., and J. D. designed the research. N. C. H. and R. S. S. performed the simulations. J. D. directed the research. N. C. H., R. S. S., and J. D. conducted the analyses and wrote the manuscript.

## Conflicts of interest

There are no conflicts to declare.

## Data availability

Data for this article, including simulation trajectories, are available at the Materials Data Facility https://doi.org/10.18126/tykw-5q20.[71,72]

Supplementary information (SI) is available. See DOI: https://doi.org/10.1039/d5me00092k.

## Acknowledgements

This research was conducted with support from the Cornell University Center for Advanced Computing (CAC), which receives funding from Cornell University, the National Science Foundation, and members of its Partner Program. R. S. S. acknowledges support from the National Science Foundation Graduate Research Fellowship grant no. DGE-2139899.

## References

1 R. K. Cersonsky, J. Antonaglia, B. D. Dice and S. C. Glotzer, *Nat. Commun.*, 2021, **12**, 2543.
2 Z. Cai, Z. Li, S. Ravaine, M. He, Y. Song, Y. Yin, H. Zheng, J. Teng and A. Zhang, *Chem. Soc. Rev.*, 2021, **50**, 5898–5951.
3 W. Zhou, Y. Li, K. Je, T. Vo, H. Lin, B. E. Partridge, Z. Huang, S. C. Glotzer and C. A. Mirkin, *Science*, 2024, **383**, 312–319.
4 N. Li, J. Li, L. Qing, S. Ma, Y. Li and B. Li, *Soft Matter*, 2024, **20**, 304–314.
5 M. A. Boles, M. Engel and D. V. Talapin, *Chem. Rev.*, 2016, **116**, 11220–11289.
6 P. F. Damasceno, M. Engel and S. C. Glotzer, *Science*, 2012, **337**, 453–457.
7 N. R. Jana, *Angew. Chem.*, 2004, **116**, 1562–1566.
8 M. H. Huang and P. Lin, *Adv. Funct. Mater.*, 2011, **22**, 14–24.
9 Z. Quan and J. Fang, *Nano Today*, 2010, **5**, 390–411.
10 D. Doan, J. Kulikowski and W. X. Gu, *Nat. Commun.*, 2024, **15**, 1954.
11 T. Kang, J. Zhu, X. Luo, W. Jia, P. Wu and C. Cai, *Anal. Chem.*, 2021, **93**, 2519–2526.
12 S. Zhou, J. Li, J. Lu, H. Liu, J.-Y. Kim, A. Kim, L. Yao, C. Liu, C. Qian, Z. D. Hood, X. Lin, W. Chen, T. E. Gage, I. Arslan, A. Travesset, K. Sun, N. A. Kotov and Q. Chen, *Nature*, 2022, **612**, 259–265.
13 D. Wang, M. Hermes, S. Najmr, N. Tasios, A. Grau-Carbonell, Y. Liu, S. Bals, M. Dijkstra, C. B. Murray and A. van Blaaderen, *Nat. Commun.*, 2022, **13**, 6001.
14 C. Liu, A. D. S. Duraes, E. L. Jiao and W. Zhang, *MRS Adv.*, 2024, **9**, 1102–1108.
15 M. R. Khadilkar and F. A. Escobedo, *Soft Matter*, 2016, **12**, 1506–1516.
16 D. Wang, T. Dasgupta, E. B. van der Wee, D. Zanaga, T. Altantzis, Y. Wu, G. M. Coli, C. B. Murray, S. Bals, M. Dijkstra and A. van Blaaderen, *Nat. Phys.*, 2021, **17**, 128–134.
17 E. G. Teich, G. van Anders, D. Klotsa, J. Dshemuchadse and S. C. Glotzer, *Proc. Natl. Acad. Sci. U. S. A.*, 2016, **113**, E669–E678.
18 R. S. Skye, E. G. Teich and J. Dshemuchadse, *Soft Matter*, 2022, **18**, 6782–6790.
19 F. Lu, Y. Zhang, T. Dwyer, A. Michelson, T. C. Moore, H. Yan, K. Kisslinger, H. Zhang, X. Chen, S. C. Glotzer and O. Gang, *Nat. Mater.*, 2025, 785–793.
20 G. Bordia, T. P. Russell and A. K. Omar, *ACS Nano*, 2025, **19**, 38803–38813.
21 C. Jenewein, J. Avaro, C. Appel, M. Liebi and H. Cölfen, *Angew. Chem., Int. Ed.*, 2022, **61**, e202112461.
22 Y. Kim, R. J. Macfarlane, M. R. Jones and C. A. Mirkin, *Science*, 2016, **351**, 579–582.

 

23 Y. Wan, Z. Cai, L. Xia, L. Wang, Y. Li, Q. Li and X. Zhao, *Mater. Lett.*, 2009, **63**, 2078–2081.
24 I. Cherniukh, G. Rainò, T. V. Sekh, C. Zhu, Y. Shynkarenko, R. A. John, E. Kobiyama, R. F. Mahrt, T. Stöferle, R. Erni, M. V. Kovalenko and M. I. Bodnarchuk, *ACS Nano*, 2021, **15**, 16488–16500.
25 B. Ni, G. Gonzalez-Rubio and H. Cölfen, *Acc. Chem. Res.*, 2022, **55**, 1599–1608.
26 S. Lin, H. Guan, Y. Liu, S. Huang, J. Li, W. Hasi, Y. Xu, J. Zou and B. Dong, *ACS Appl. Mater. Interfaces*, 2021, **13**, 53289–53299.
27 M. R. Khadilkar and F. A. Escobedo, *J. Chem. Phys.*, 2012, **137**, 194907.
28 A. T. Cadotte, J. Dshemuchadse, P. F. Damasceno, R. S. Newman and S. C. Glotzer, *Soft Matter*, 2016, **12**, 7073–7078.
29 A.-P. Hynninen, J. H. Thijssen, E. C. Vermolen, M. Dijkstra and A. van Blaaderen, *Nat. Mater.*, 2007, **6**, 202–205.
30 Z. Cai, J. Teng, Y. Wan and X. Zhao, *J. Colloid Interface Sci.*, 2012, **380**, 42–50.
31 J. Liu, Y. Cai, Y. Deng, Z. Sun, D. Gu, B. Tu and D. Zhao, *Microporous Mesoporous Mater.*, 2010, **130**, 26–31.
32 U. Agarwal and F. A. Escobedo, *Nat. Mater.*, 2011, **10**, 230–235.
33 M. R. Khadilkar, U. Agarwal and F. A. Escobedo, *Soft Matter*, 2013, **9**, 11557.
34 M. R. Khadilkar and F. A. Escobedo, *Phys. Rev. Lett.*, 2014, **113**, 165504.
35 J. Henzie, M. Grünwald, A. Widmer-Cooper, P. L. Geissler and P. Yang, *Nat. Mater.*, 2011, **11**, 131–137.
36 M. Eguchi, D. Mitsui, H.-L. Wu, R. Sato and T. Teranishi, *Langmuir*, 2012, **28**, 9021–9026.
37 S.-C. Lu, M.-C. Hsiao, M. Yorulmaz, L.-Y. Wang, P.-Y. Yang, S. Link, W.-S. Chang and H.-Y. Tuan, *Chem. Mater.*, 2015, **27**, 8185–8188.
38 Z. L. Wang and X. Feng, *J. Phys. Chem. B*, 2003, **107**, 13563–13566.
39 Y. Zheng, W. Liu, T. Lv, M. Luo, H. Hu, P. Lu, S.-I. Choi, C. Zhang, J. Tao, Y. Zhu, Z.-Y. Li and Y. Xia, *Chem. – Asian J.*, 2014, **9**, 2635–2640.
40 M. X. He, J. P. Gales, E. Ducrot, Z. Gong, G. R. Yi, S. Sacanna and D. J. Pine, *Nature*, 2020, **585**, 524–529.
41 Y. Nagaoka, H. Zhu, D. Eggert and O. Chen, *Science*, 2018, **362**, 1396–1400.
42 HOOMD-blue, https://hoomd-blue.readthedocs.io.
43 J. A. Anderson, C. D. Lorenz and A. Travesset, *J. Comput. Phys.*, 2008, **227**, 5342–5359.
44 J. A. Anderson, M. Eric Irrgang and S. C. Glotzer, *Comput. Phys. Commun.*, 2016, **204**, 21–30.
45 J. A. Anderson, J. Glaser and S. C. Glotzer, *Comput. Mater. Sci.*, 2020, **173**, 109363.
46 G. van Anders, D. Klotsa, N. K. Ahmed, M. Engel and S. C. Glotzer, *Proc. Natl. Acad. Sci. U. S. A.*, 2014, **111**, E4812–E4821.
47 G. van Anders, N. K. Ahmed, R. Smith, M. Engel and S. C. Glotzer, *ACS Nano*, 2014, **8**, 931–940.
48 E. S. Harper, G. van Anders and S. C. Glotzer, *Proc. Natl. Acad. Sci. U. S. A.*, 2019, **116**, 16703–16710.
49 G. Bryant, S. R. Williams, L. Qian, I. K. Snook, E. Perez and F. Pincet, *Phys. Rev. E*, 2002, **66**, 060501.
50 C. S. Adorf, V. Ramasubramani, B. D. Dice, M. M. Henry, P. M. Dodd and S. C. Glotzer, glotzerlab/signac, 2019, DOI: 10.5281/zenodo.2581327.
51 C. S. Adorf, P. M. Dodd, V. Ramasubramani and S. C. Glotzer, *Comput. Mater. Sci.*, 2018, **146**, 220–229.
52 V. Ramasubramani, C. S. Adorf, P. M. Dodd, B. D. Dice and S. C. Glotzer, Proceedings of the 17th Python in Science Conference, 2018, pp. 152–159.
53 https://freud.readthedocs.io.
54 V. Ramasubramani, B. D. Dice, E. S. Harper, M. P. Spellings, J. A. Anderson and S. C. Glotzer, *Comput. Phys. Commun.*, 2020, **254**, 107275.
55 A. Stukowski, OVITO, https://www.ovito.org.
56 A. Stukowski, *Modell. Simul. Mater. Sci. Eng.*, 2010, **18**, 015012.
57 https://plato-draw.readthedocs.io.
58 D. Frenkel and B. Smit, *Understanding Molecular Simulation: From Algorithms to Applications*, Academic Press, 2002.
59 L. Filion, M. Marechal, B. van Oorschot, D. Pelt, F. Smallenburg and M. Dijkstra, *Phys. Rev. Lett.*, 2009, **103**, 188302.
60 J. R. Espinosa, C. Vega, C. Valeriani, D. Frenkel and E. Sanz, *Soft Matter*, 2019, **15**, 9625–9631.
61 A. Haji-Akbari, M. Engel, A. S. Keys, X. Zheng, R. G. Petschek, P. Palffy-Muhoray and S. C. Glotzer, *Nature*, 2009, **462**, 773–777.
62 R. A. LaCour, T. C. Moore and S. C. Glotzer, *Phys. Rev. Lett.*, 2022, **128**, 188001.
63 E. G. Teich, G. van Anders and S. C. Glotzer, *Nat. Commun.*, 2019, **10**, 64.
64 B. de Nijs, S. Dussi, F. Smallenburg, J. D. Meeldijk, D. J. Groenendijk, L. Filion, A. Imhof, A. van Blaaderen and M. Dijkstra, *Nat. Mater.*, 2015, **14**, 56–60.
65 T. Einert, P. Lipowsky, J. Schilling, M. J. Bowick and A. R. Bausch, *Langmuir*, 2005, **21**, 12076–12079.
66 U. T. Lieu and N. Yoshinaga, *Soft Matter*, 2020, **16**, 7667–7675.
67 D. Wang, M. Hermes, R. Kotni, Y. Wu, N. Tasios, Y. Liu, B. de Nijs, E. B. van der Wee, C. B. Murray, M. Dijkstra and A. van Blaaderen, *Nat. Commun.*, 2018, **9**, 2228.
68 B. S. John, A. Stroock and F. A. Escobedo, *J. Chem. Phys.*, 2004, **120**, 9383–9389.
69 J. W. Wang, C. F. Mbah, T. Przybilla, B. A. Zubiri, E. Spiecker, M. Engel and N. Vogel, *Nat. Commun.*, 2018, **9**, 5259.
70 L. Li, C. Goodrich, H. Yang, K. R. Phillips, Z. Jia, H. Chen, L. Wang, J. Zhong, A. Liu, J. Lu, J. Shuai, M. P. Brenner, F. Spaepen and J. Aizenberg, *Proc. Natl. Acad. Sci. U. S. A.*, 2021, **118**, e2107588118.
71 B. Blaiszik, K. Chard, J. Pruyne, R. Ananthakrishnan, S. Tuecke and I. Foster, *JOM*, 2016, **68**, 2045–2052.
72 N. C. Huang, R. S. Skye and J. Dshemuchadse, Advancing the Self-Assembly of Binary Colloidal Crystals of Tetrahedra and Octahedra with Confinement, DOI: 10.18126/tykw-5q20, 2025.